

# 1 Preliminary studies

## 1.1 Homogeneous vs heterogeneous isotope distribution

In this section, we conducted a study to determine the proper way to treat the fuel compact heterogeneities. This study modeled two different isotope distributions in a fuel compact. First, a homogeneous distribution of the isotopes. Second, a heterogeneous distribution, in which we explicitly modeled the TRISO particles. We modeled both cases using Serpent. We used a hexagonal unit cell model that includes the fuel compact, a helium gap, and the surrounding graphite. Table ?? specifies the model input parameters. The material temperature was 1200K, a case that represents the Hot Full Power (HFP) core state. Serpent ran  $5 \times 10^4$  neutrons/cycle, 500 active cycles, and 50 inactive cycles for the calculations. The simulations took 1.73 and 2.21 minutes using 256 cores. The heterogeneous calculation took 28%.

The multiplication factor ( $K_{eff}$ ) was 1.17523 for the homogeneous case and 1.25106 for the heterogeneous case. Using the heterogeneous case as the reference result, we calculated the most relevant group constants' relative error in an eigenvalue calculation. Serpent generated the group constants using the three energy group structure in Table 2. The evaluated parameters were  $D_g$ ,  $\Sigma_g^r$ ,  $v\Sigma_g^f$ , and  $\chi_g^t$  (see equation ??). Figure 1 displays the relative errors for  $\Sigma_g^r$  (REMXS) and  $v\Sigma_g^f$  (NSF), which were the group constants that changed the most. The figure does not include relative errors for  $D_g$  and  $\chi_g^t$  because they were less than 1%. The relative errors of  $\Sigma_g^r$  and  $v\Sigma_g^f$  were less than 6%.

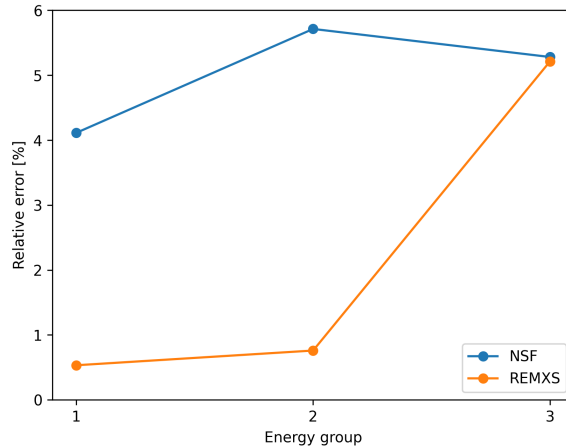


Figure 1: Relative error of the group constants generated with a homogeneous isotope distribution.

The results showed that the multiplication factor decreases considerably. The homogenization of the fuel compact isotopes appears not to have a substantial impact on the group constants. However, the considerable difference in the multiplication factor suggests that the group constants' small variations combined effect is significant. Based on these results, Serpent models the TRISO particles explicitly in the following sections.

## 1.2 Moltres limitations

Diffusion calculations necessitate a homogenization in space of group constants. Depending on the desired level of detail, the type of homogenization could vary. For example, in PWR core calculations the homogenization in space could be per assembly or pin-by-pin [?]. In a per assembly homogenization, the diffusion code models a global neutronic representation of the assembly. A pin-by-pin calculation makes possible the treatment of pin or assembly heterogeneities. This type of calculation yields a detailed neutronic representation of the fuel pins. As the former treats a larger region and gives a more homogeneous solution, it is often called homogeneous calculation. The latter allows for the treatment of some heterogeneities and we will refer to it as a heterogeneous

calculation.

Moltres is a heterogeneous solver and is capable of yielding detailed answers. Previous works [2][5] have analyzed Molten Salt Reactors (MSRs). In such calculations, Moltres input files defined essentially two materials: the moderator and the fuel. With such a heterogeneous configuration, a node in the mesh representing the moderator holds the information of the neutronics and temperature only for the moderator. The same is true for the fuel. A homogeneous calculation does not differentiate between moderator and fuel and holds the information of both materials in each node.

Keeping in mind the previous work in Moltres, we aimed for a heterogeneous calculation in a prismatic High Temperature Gas-Cooled Reactor (HTGR). For such calculation, we modeled a fuel column of the MHTG-350 and generate the group constants using Serpent. Figure 2 displays Serpent model geometry. We obtained the group constants for three materials: moderator, coolant, and fuel compact. Serpent run  $5 \times 10^5$  neutrons/cycle, 400 active cycles, and 100 inactive cycles for the calculations.

Taking advantage of the symmetry of the problem, Moltres model included only a one-twelfth of the fuel column, Figure 2. We made the geometry and mesh using Gmsh [1]. The diffusion calculations had 183667 degrees of freedom (DoFs)/energy-group. The Moltres input files set an eigenvalue and a flux convergence tolerance of  $1 \times 10^{-8}$ . The calculations in Moltres used a two group structure with a thermal cutoff at 0.625eV. The eigenvalue calculation did not converge. Several factors could contribute to this phenomenon. We focused on the validity of the diffusion calculations in such system.

The diffusion theory considers the current density is proportional to the gradient of the flux [?]. Such an approximation relies on the following assumptions:

- The angular flux does not depend strongly on the angular variables.
- The fission source is isotropic.
- The time derivative of the current density is small compared to the mean collision time.
- The anisotropic energy-transfer contribution can be ignored in group-to-group scattering.

More detailed studies of the transport equation indicate that the following cases violate the assumption of a weak angular dependence [?]:

- near vacuum boundaries and low-density material regions
- near strongly absorbing media
- near localized sources

The diffusion theory applies best to geometries consisting of large homogeneous material regions where the spatial dependence of the neutron flux is not too strong, i.e. where the flux gradient is small. This is the case for material regions whose geometrical scales are larger than the neutron mean free path. For this reason, we compared the neutron mean free path in the different fuel assembly materials, Table 1. The mean free path in the fuel and the moderator are in the order of the centimeters. In the coolant, the mean free path has a comparable magnitude to the fuel column dimensions. This results suggest that a heterogeneous diffusion calculation of the prismatic fuel column violates the diffusion theory assumptions.

Moving forward, we opt for a homogeneous representation of the fuel assembly. Serpent calculated the homogeneous group constants.

In order to compare the solutions from both codes, we compare their results. Serpent's  $K_{eff}$  was 1.41933 while Moltres' was 1.4078788. Additionally, we obtained the axial flux in the fuel column. Serpent's flux is an average over the fuel column volume. Moltres flux is the point-wise flux over the z-axis. Figure 3 displays a comparison between Serpent and Moltres axial fluxes. We empathize that this was a feasibility study, and the following sections make a deeper analysis of similar results.

Based on these results and discussion, in the following sections, we obtain the group constants using the homogeneous scheme. In the fuel assembly, the fuel, coolant, and moderator all share the same group constants.

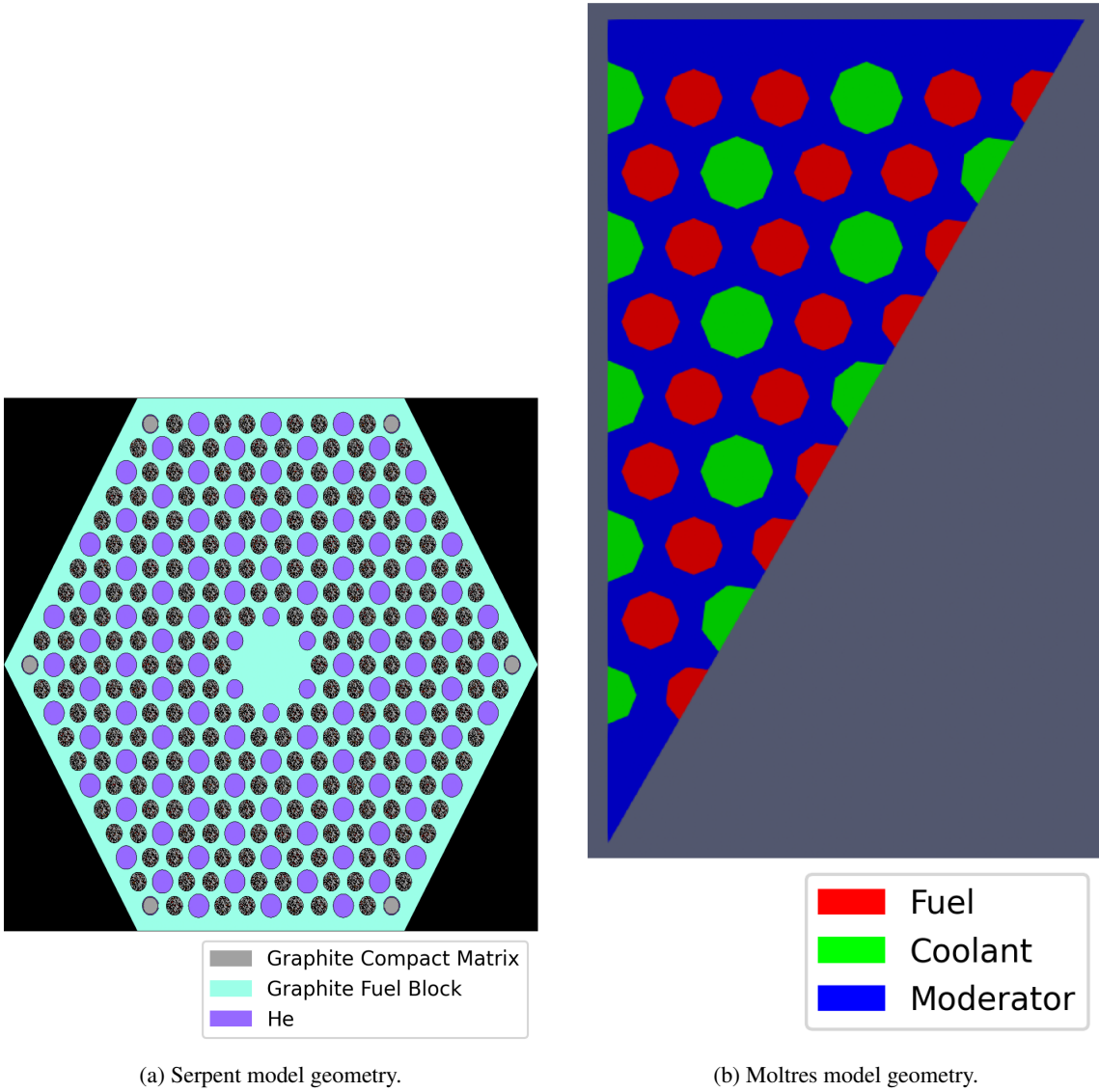


Figure 2: Fuel column of the MHTGR-350. XY-plane in the active core region.

Table 1: Mean free path in different materials. Values expressed in *cm*.

	Fuel compact	Moderator	Coolant	Homogeneous fuel
Fast	2.71	2.70	1137.31	3.37
Thermal	2.22	2.36	1945.49	2.89

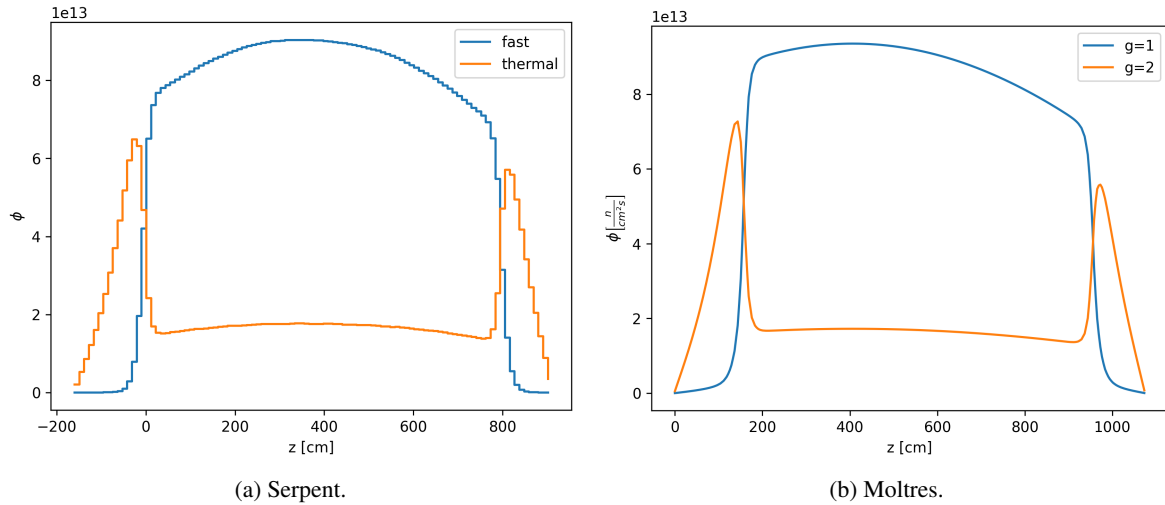


Figure 3: Two group axial flux comparison.

## 2 Serpent-Moltres comparison

### 2.1 Fuel column

In this section, we investigated the effects of the energy group structure on the diffusion simulations. We conducted two analyses. First, we varied the number of energy groups. Second, we tried different energy group structures for the same number of groups. To reduce the computational expense, we narrowed down our focus to a fuel column of the MHTGR-350, Figure 2. The fuel column includes the bottom and top reflectors. Tables ?? and ?? specify the model input parameters.

The first step in the calculation was to obtain the group constants using Serpent. Figure 2 displays a  $xy$ -plane of the model. To simplify Serpent’s model, we did not consider the fuel handling holes or the bottom and top reflectors’ coolant channels. HTGRs use lumped burnable poisons (LBPs) to reduce the power peaking factors in different active core regions. Some reactors could have LBPs in the rings closer to the reflectors, and no LBPs in the middle rings. This characteristic motivated the analysis of two cases, a fuel column that does not have LBPs, and one that has. The LBP’s locations are the six corners of the fuel assembly, Figure ???. The material temperatures were 600K and 1200K, cases that represent the Cold Zero Power (CZP) and the HFP core states. Serpent ran  $4 \times 10^5$  neutrons/cycle, 360 active cycles, and 40 inactive cycles for the calculations.

Taking advantage of the symmetry of the problem, the Moltres model included only a one-twelfth of the fuel column. We made the geometry and mesh using Gmsh [1]. The mesh had 37120 elements and 22862 nodes. The diffusion calculations had 22862 DoFs/energy-group. The Moltres input files set an eigenvalue and a flux convergence tolerance of  $1 \times 10^{-8}$ . The calculations in Moltres used different energy group structures listed in Table 2.

To compare the results from Serpent and Moltres, we present a figure comparing the three-group axial flux. Moltres ran the calculations for 26 energy groups, and collapsed the results to three energy groups to facilitate the visualization of the results. Note that the flux in Serpent is an average over the volume, while the flux in Moltres is the point-wise flux over a line. Another figure compares the eigenvalue from Serpent and eigenvalues from Moltres for the different energy group structures. The last analysis is for the Moltres axial flux. Considering the 26 group structure as the reference value, we obtained the L2-norm relative error for the axial flux in the active core.

To recapitulate, we simulated four operational cases: no LBP at 600K, no LBP at 1200K, LBP at 600K, and LBP at 1200K. Figures 4 to 7 display the axial flux from the Serpent and the Moltres simulations for all cases.

For the no LBP at 600K case, the fluxes are close in shape and magnitude. For the no LBP at 1200K case, the fluxes look similar. The flux in Moltres has a more straight shape. The thermal flux peak in the bottom reflector has a bigger magnitude. For the LBP at 600K case, the flux in Moltres has a bigger magnitude. Additionally, the shape of the Moltres flux is concave while the Serpent flux is convex. For the LBP at 1200K case, the flux in Moltres is bigger. The Moltres flux is more concave than the Serpent flux. Overall, the fluxes in Moltres and Serpent are close.

Table 3 exhibits the reactivity difference ( $\Delta\rho$ ) between the Serpent and Moltres eigenvalues. We used equation 1 to obtain  $\Delta\rho$ . The eigenvalues in Moltres differ slightly from the eigenvalues in Serpent. Overall, the reactivity difference is less than 50 pcm. We note that the number of energy groups does not affect the accuracy of the eigenvalue calculations in Moltres.

$$\Delta\rho = \left| \frac{k_1 - k_2}{k_1 k_2} \right| \quad (1)$$

where

$$\begin{aligned} k_1 &= \text{Serpent eigenvalue} \\ k_2 &= \text{Moltres eigenvalue.} \end{aligned}$$

Figures 8 and 9 show the  $L_2$ -norm relative error for the different energy group structures. We note that the relative error for the no LBP case is smaller than the relative error of the LBP case. Overall, the relative error decreases with an increase in the number of energy groups. Nonetheless, this is not always the case. For example, in Figure 8b, going from 12 to 15 groups, the thermal flux improves, but the fast flux worsens. Additionally, we observe that a low number of energy groups yields an error of more than a 100%. In which, case we can conclude that the solution is wrong.

We added to the analysis the computational time and the peak memory usage during the simulations, Figure 10. All the simulations used 128 cores. We present only the cases at 600K because the change in temperature does not have a significant impact. The computational requirements rises with an increase in the number of energy groups. As the geometry uses a constant number of elements, the DoFs/energy-group is constant. Thus, the total number of DoFs is proportional to the number of energy groups. We also discern that the overall time of the LBP cases is higher than the no LBP cases.

Finally, we analyzed the impact of changing the energy group structure for a constant number of energy groups. We chose 15 energy groups, as it gives an overall good accuracy and a not so high computational expense.

Table 2 holds the different energy group structures. Table 4 exhibits the  $L_2$ -norm relative error for the different energy group structures. We see that the energy group structure has an impact over the accuracy. Some energy groups structures yield better results for some cases while giving worse results for others. For example, the structure 15d gives better results for the LBP at 600K case than for the no LBP case at 600K. In order to choose the best performing structure, we used a weighted average for the different groups. We arbitrarily chose the weights to be 0.5, 0.3, and 0.2 for the thermal, epithermal, and fast fluxes. Using this averaging scheme, we determined the group structure 15d to be the best one.

## 2.2 Full-core

In this section, we compared the results from Serpent and Moltres for a full-core simulation. The first step in the calculation was to obtain the group constants using Serpent. Figure 11 displays the  $xy$ -plane of the model. The model includes the bottom and top reflectors. Tables ??, ?? and ?? specify the model input parameters. To simplify Serpent's model, all the fuel columns were standard fuel columns. Additionally, the model does not include the fuel handling holes nor the coolant channels in the bottom and top reflectors. The model considered

Table 2: Energy group structure.

Upper boundary [eV]	26	21	18	15a	15b	15c	15d	15e	12	9	6	3
1.49E+07	1	1	1	1	1	1	1	1	1	1	1	1
7.41E+06	2											
3.68E+06	3	2	2	2	2	2	2	2	2			
6.72E+05	4											
1.11E+05	5	3	3	3	3	3	3	3	3	2	2	2
1.93E+04	6	4	4	4	4					4		
3.35E+03	7											
1.58E+03	8	5	5									
7.48E+02	9	6	6	5	5					5	3	
2.75E+02	10	7	7	6	6	5			6	4		
1.30E+02	11	8	8	7	7				7	5	3	
6.14E+01	12	9				8	6					
2.90E+01	13	10	9	8		9			6			
1.37E+01	14	11	10	9						8	6	
8.32E+00	15	12	11	10	10				9			
5.04E+00	16											
2.38E+00	17	13	12	11	11	8	8	8	10	7	4	3
1.29E+00	18	14										
6.50E-01	19	15	13	12	12	9	9	9	11	8	5	
3.50E-01	20	16				10	10					
2.00E-01	21	17	14	13	13	11	11	10				
1.20E-01	22							11				
8.00E-02	23	18	15	14	14	12	12	12				
5.00E-02	24	19	16			13	13	13				
2.00E-02	25	20	17	15	15	14	14	14	12	9	6	
1.00E-02	26	21	18			15	15	15				

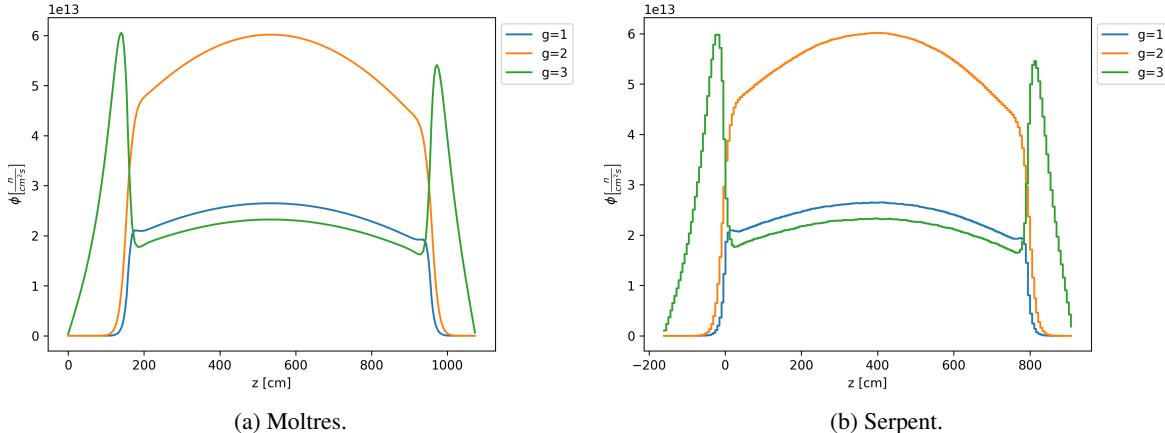
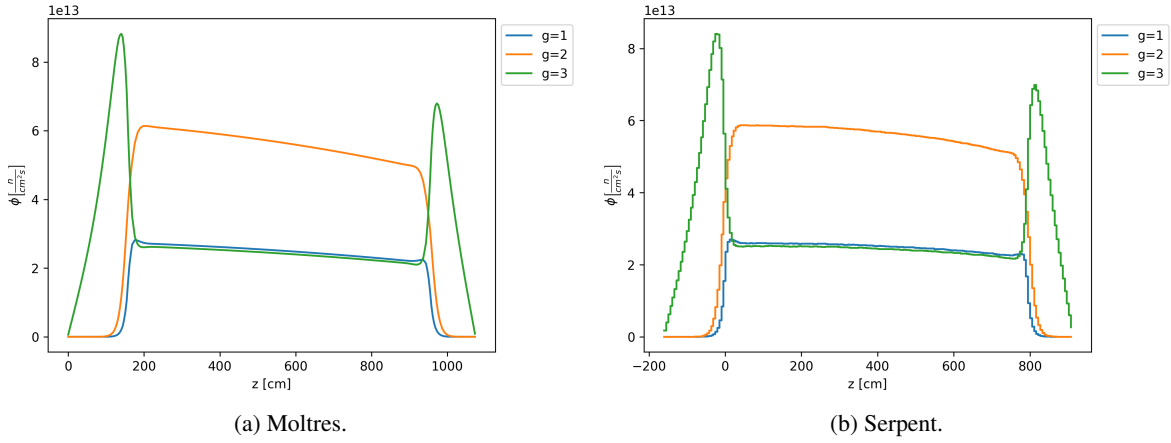
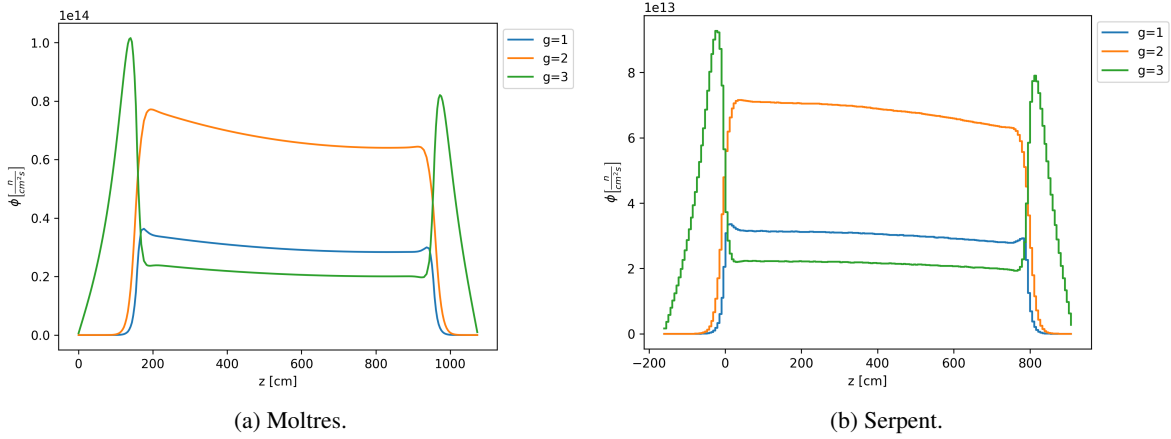


Figure 4: Case no LBP at 600K. 3-group axial neutron flux.



(a) Moltres. (b) Serpent.

Figure 5: Case no LBP at 1200K. 3-group axial neutron flux.



(a) Moltres. (b) Serpent.

Figure 6: Case LBP at 600K. 3-group axial neutron flux.

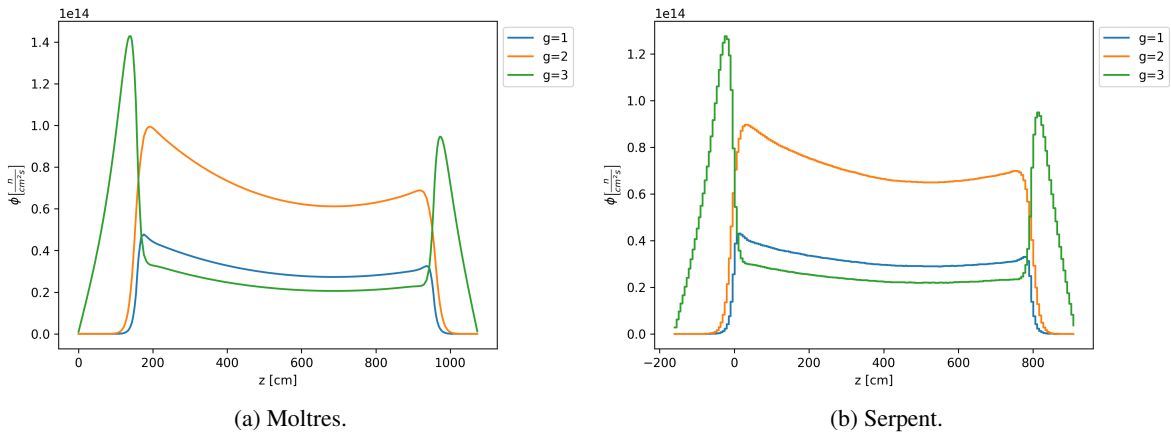


Figure 7: Case LBP at 1200K. 3-group axial neutron flux.

Table 3: Serpent and Moltres eigenvalues.

	Serpent	$\Delta\rho$ [pcm]							
		3	6	9	12	15	18	21	26
no LBP, 600K	1.43800	10	7	6	6	5	6	6	12
no LBP, 1200K	1.37771	23	15	4	3	2	2	1	11
LBP, 600K	1.12861	44	21	24	25	25	24	19	9
LBP, 1200K	1.06554	36	40	29	32	44	43	25	25

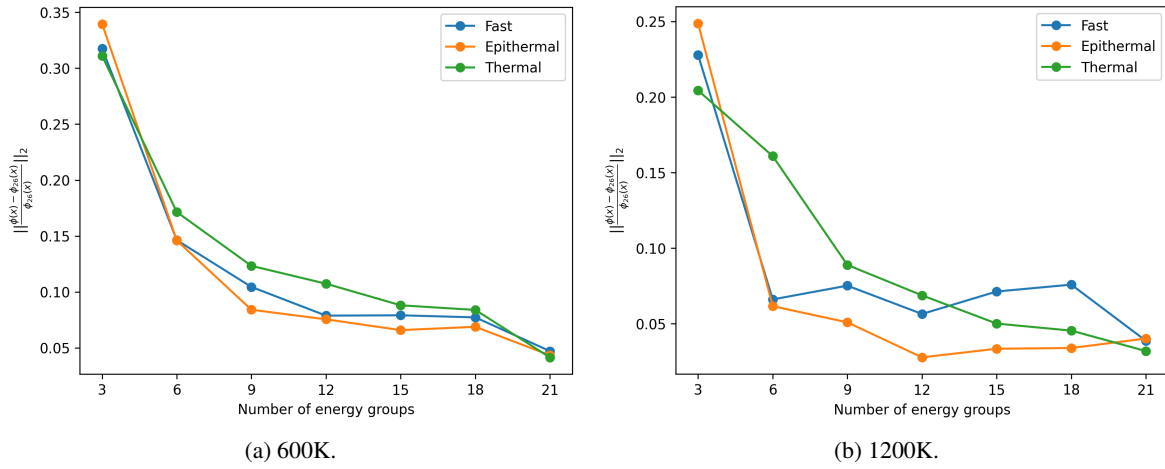


Figure 8: No LBP case. L<sub>2</sub>-norm relative error for different number of energy group structures.

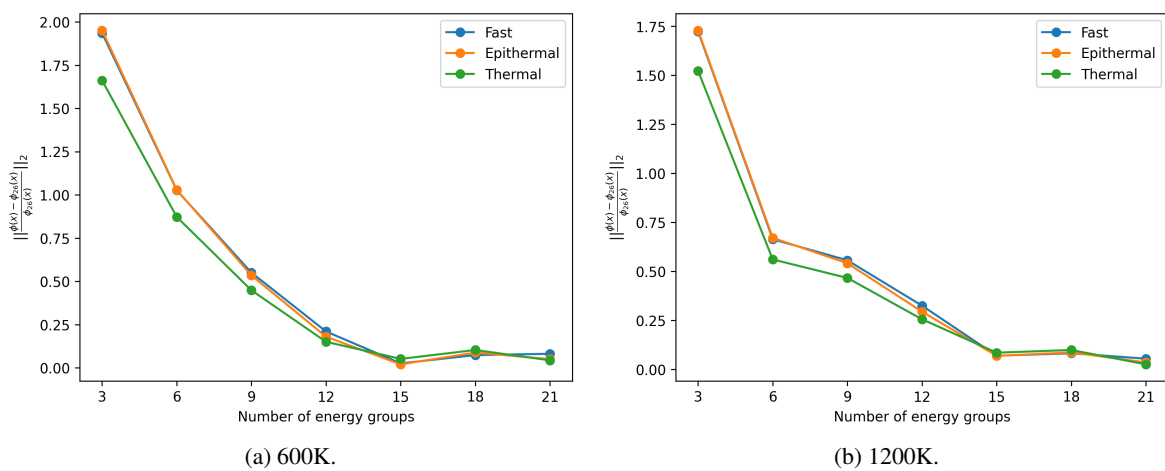


Figure 9: LBP case. L<sub>2</sub>-norm relative error for different number of energy group structures.

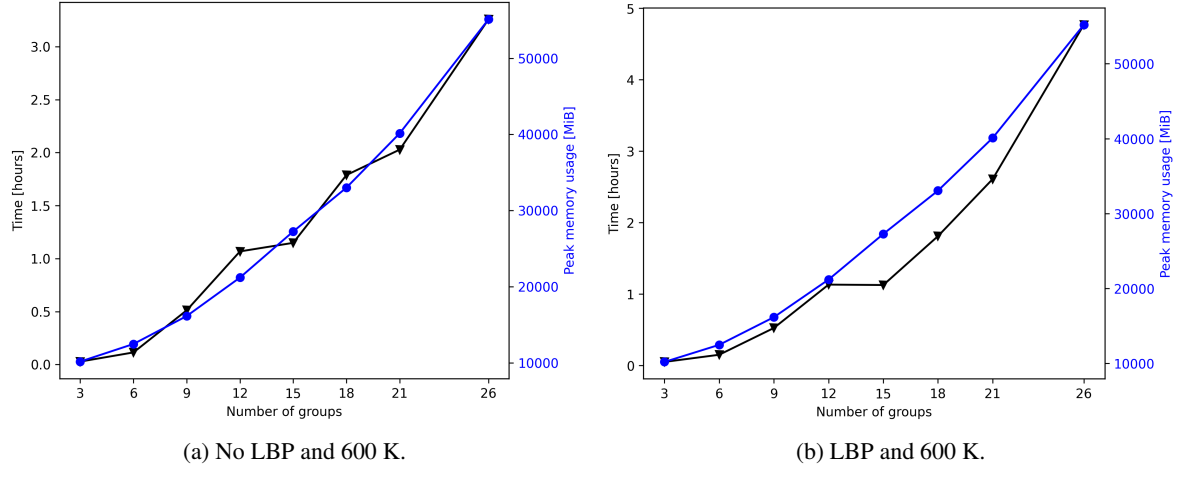


Figure 10: Computational time and memory requirements for different number of energy group structures.

Table 4:  $L_2$ -norm relative error for various energy group structures. Values expressed in percentage.

LBP	Temperature [K]	Flux	15a	15b	15c	15d	15e
No	600	Fast	7.9	8.0	8.2	8.1	9.1
		Epithermal	6.6	6.5	8.6	8.2	9.2
		Thermal	8.8	8.5	10.6	10.7	12.9
	1200	Fast	7.1	7.7	5.7	5.1	4.5
		Epithermal	3.3	3.9	6.2	5.1	3.4
		Thermal	5.0	4.7	8.5	8.2	8.4
Yes	600	Fast	24.0	24.8	2.6	2.3	3.7
		Epithermal	21.0	21.7	2.0	1.6	2.7
		Thermal	18.1	18.8	5.2	5.5	5.7
	1200	Fast	36.2	37.3	6.9	6.6	25.9
		Epithermal	33.2	34.2	6.9	6.5	25.1
		Thermal	29.6	30.6	8.5	8.3	20.3
Weighted average			17.3	17.8	6.3	6.0	10.8

a fresh core. Based on the previous section analyses, we chose the energy group structure 15d in Table 2. The material temperatures were 600K and 1200K, cases that represent the CZP and the HFP core states. Serpent ran  $8 \times 10^5$  neutrons/cycle, 500 active cycles, and 100 inactive cycles for the calculations.

For the Moltres input file, we made the geometry and mesh using Gmsh. Taking advantage of the symmetry of the problem, the model included only a one-sixth of the full-core. The mesh had 300720 elements and 160035 nodes. The diffusion calculations had 160035 DoFs/energy-group, and a total of 2400525 DoFs. The Moltres input files set an eigenvalue and a flux convergence tolerance of  $1 \times 10^{-8}$ .

Between Serpent and Moltres, we compared the  $K_{eff}$ , the power distribution, and the flux shape and magnitude in different zones of the reactor. Table 5 exhibits the  $K_{eff}$  from Serpent and Moltres. Moltres values are larger than Serpent's. The values are within a 300 pcm difference.

Figures 12 and 13 show Serpent and Moltres radial power distributions. The following analysis applies for both temperatures. The first thing that came to our attention is the symmetry of the power distribution. The results are symmetric with respect to a  $60^\circ$  line. This result suggests that we could reduce the mesh size by a half by considering only a one-twelfth of the reactor. The next observation is that Moltres exhibits a higher power density than Serpent in the inner ring and outer rings. The power density in the middle ring is lower for Moltres case. The largest difference is in the inner ring. Overall, the results differ in less than 0.30 MW.

To compare the fluxes, we placed an axial and a radial flux detectors in arbitrary regions of the reactor. Figure 14 shows the location of the detectors. Note that the flux in Serpent is an average over the volume, while the flux in Moltres is the point-wise flux over a line. The Serpent axial detector's volume was the fuel column's volume. The Moltres axial detector's location was the center of the fuel column. The Serpent radial detector's volume had a  $2^\circ$ -angle and a fuel assembly's height. Both Serpent and Moltres radial detector's location was the middle of the active core's height. Moltres ran the calculations for 15 energy groups, and collapsed the results to three groups to facilitate the visualization of the results. Figures 15 and 16 show the axial and radial fluxes at 600K. In Figure 15, the fast and epithermal fluxes in Moltres are larger while the thermal flux is smaller. The flux shapes are similar. The epithermal and thermal fluxes are closer in magnitude in the active core in Serpent's simulation. In Figure 16, Serpent fluxes present some 'noise'. A higher number of generations/cycle in Serpent simulations would solve it. Another alternative is using a detector with a larger volume. Additionally, the flux in Serpent shows the location of the LBPs in the fuel assemblies. A diffusion solver fails to capture such localized effects as the group constants are homogeneous in the fuel assembly. Regarding the magnitude, the fast flux in Moltres is larger while the epithermal and thermal fluxes have almost the same magnitudes. Figures 17 and 18 display the fluxes at 1200K. These results are different from the 600K case. However, we observe the same behavior for both axial and radial fluxes.

Table 5: Serpent and Moltres eigenvalues.

	Serpent	Moltres	$\Delta\rho$ [pcm]
600K	1.10869	1.11150	228
1200K	1.06138	1.06468	292

### 3 OECD/NEA MHTGR-350 MW Benchmark: Phase I Exercise 1

This section conducted Phase I Exercise 1 of the benchmark with Moltres and compared the results with the already published results [4]. The benchmark specifies the cross-sections required to conduct the exercise. This ensures a common dataset among various benchmark participants. The files *OECD-MHTGR350\_Simplified\_xs* and *xsmap.pdf* specify the group constants and the constants numbering map. The benchmark definition used DRAGON-4 [3] from a full block configuration. The dataset contains 26 energy groups. The exercise requests the reporting of the global parameters:  $K_{eff}$ , control rod (CR) worth ( $\Delta\rho_{CR}$ ), and axial offset ( $AO$ ). It also

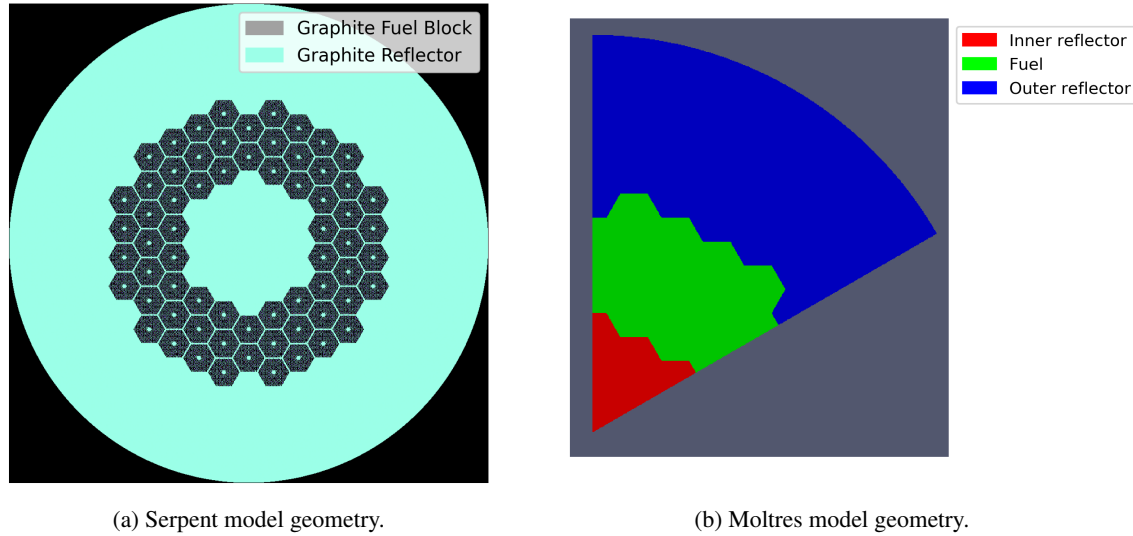


Figure 11: MHTGR-350 full-core models.

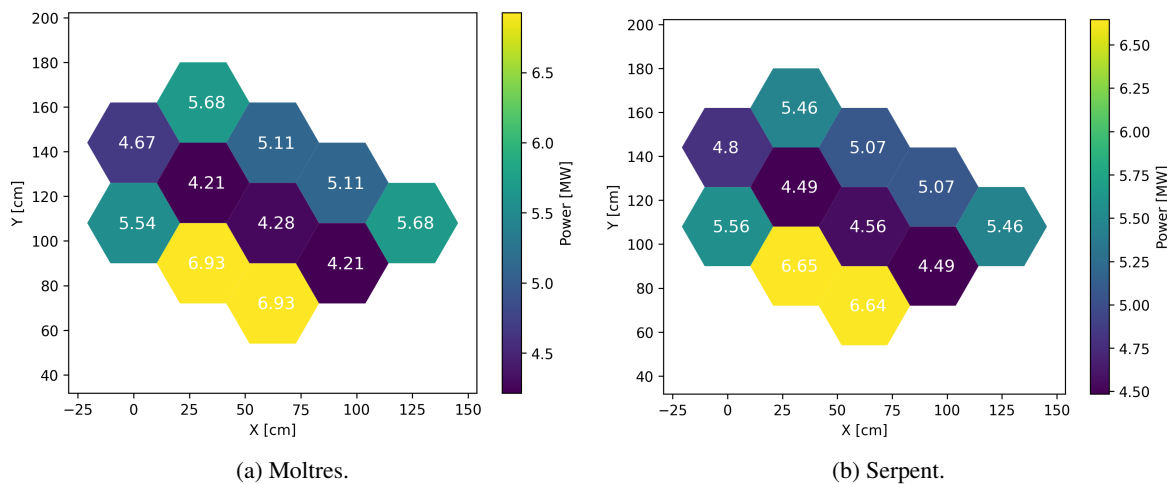


Figure 12: Radial power distribution at 600 K.

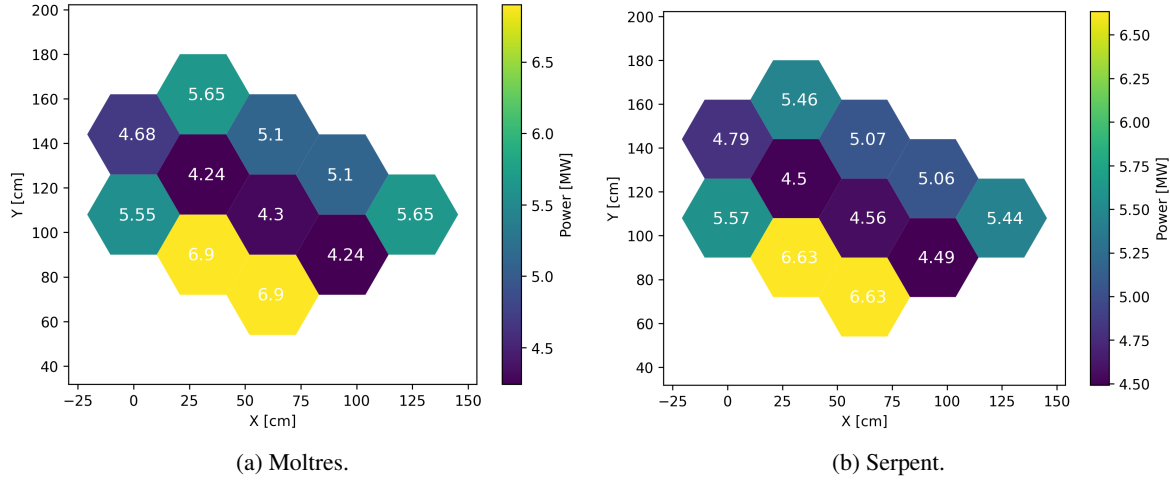


Figure 13: Radial power distribution at 1200 K.

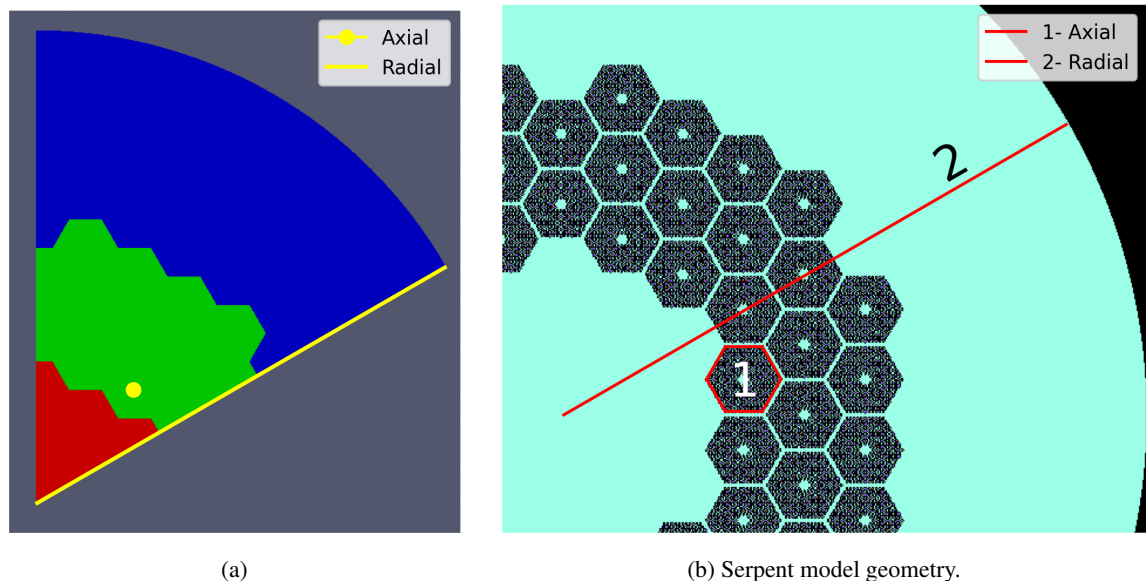


Figure 14: Flux detector locations.

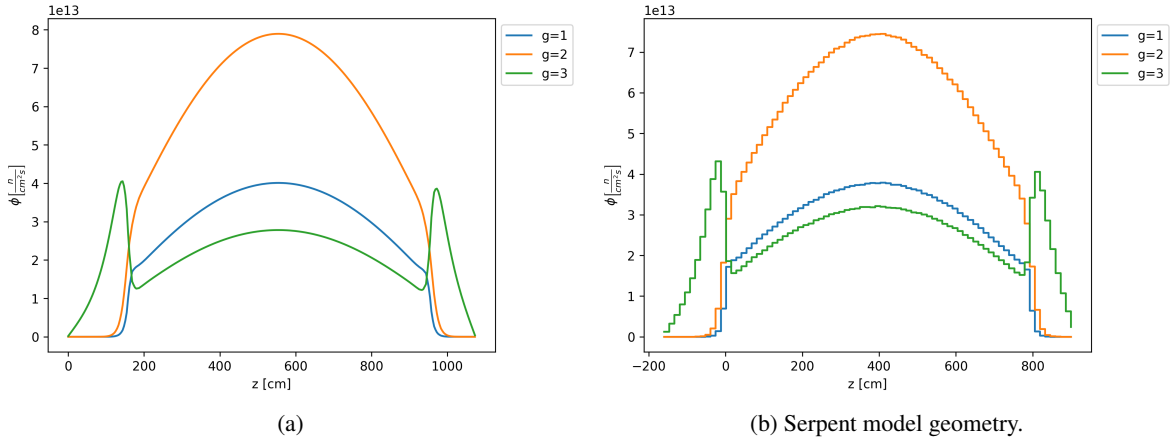


Figure 15: Axial flux at 600 K.

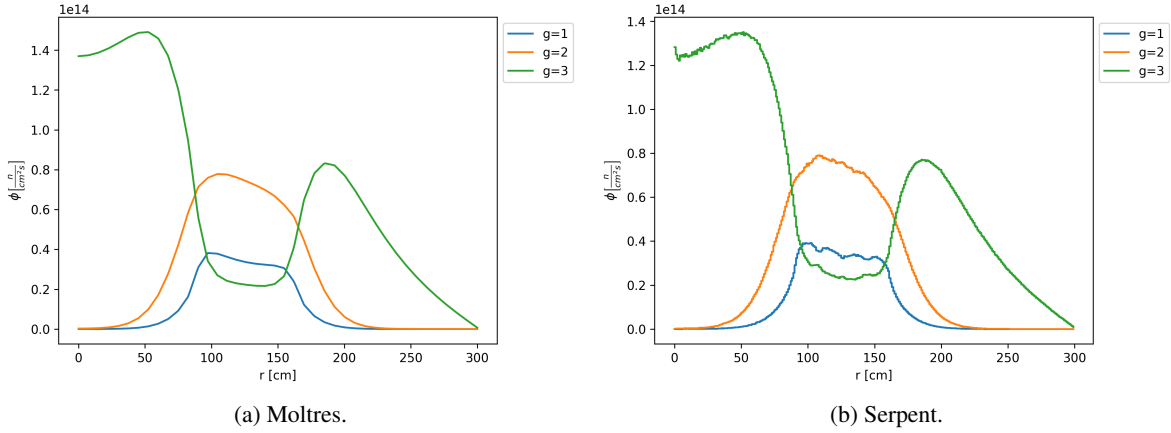


Figure 16: Radial flux at 600 K.

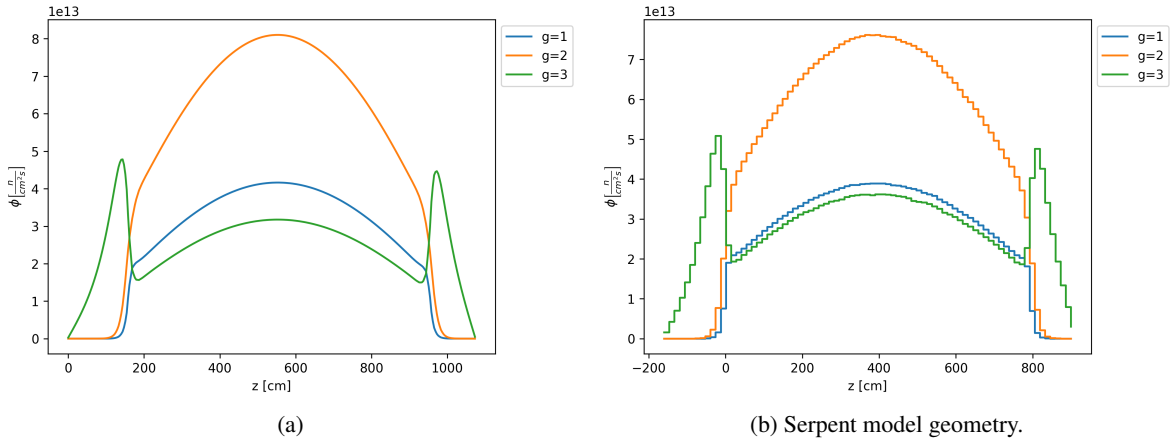


Figure 17: Axial flux at 1200 K.

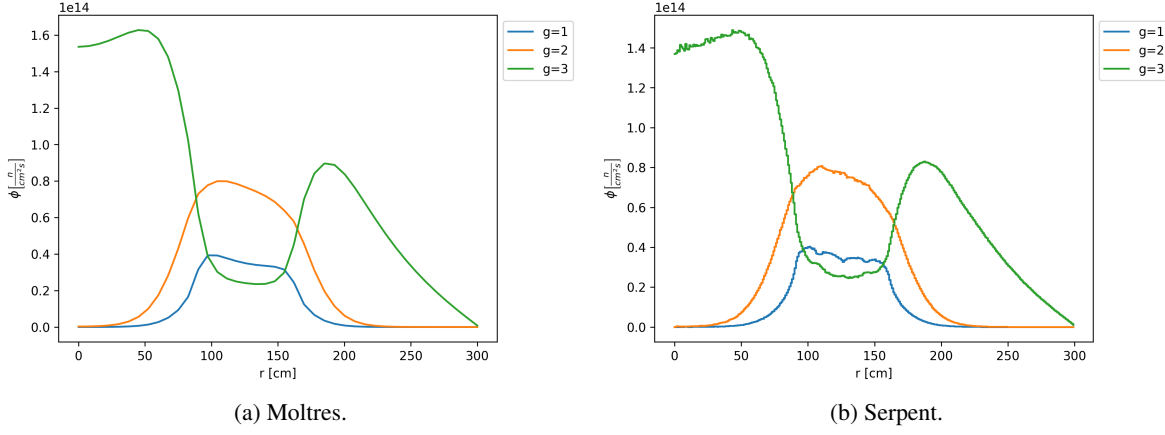


Figure 18: Radial flux at 1200 K.

requires the reporting of a power distribution map [?]. Equations 2 and 5 define  $\Delta\rho_{CR}$  and  $AO$ .

$$\Delta\rho_{CR} = \frac{k_{out} - k_{in}}{k_{out}k_{in}} \quad (2)$$

where

$$k_{out} = \text{eigenvalue with CR at position 1184.8 cm} \quad (3)$$

$$k_{in} = \text{eigenvalue with CR at position 391.81 cm} \quad (4)$$

and

$$AO = (TP_{top} - TP_{bottom}) / (TP_{top} + TP_{bottom}) \quad (5)$$

where

$$TP_{top} = \text{total power produced in the top half core} \quad (6)$$

$$TP_{bottom} = \text{total power produced in the bottom half core.} \quad (7)$$

Figure 19 displays the geometry of the MHTGR-350. The model included a one-third of the reactor. The model considered the bottom and top reflectors. The fuel consisted of 220 assemblies. The simulations required two meshes. One for the control rod out (equation 2) and one for the control rod in. The simulation with the control rod out had 268393 DoFs/energy-group, and a total of 6978218 DoFs. The simulation with the control rod in had 227592 DoFs/energy-group, and a total of 5917392 DoFs. The Moltres input files set an eigenvalue convergence tolerance of  $1 \times 10^{-8}$ .

The benchmark exercise sets periodic boundary conditions on the the sides of the geometry. However, a memory issue did not allow for the implementation of those boundary conditions in our 26-group Moltres input file. We approximated the periodic boundary condition with the reflective boundary condition. Section 3.1 discusses further on the use of periodic and reflective boundary conditions.

On average, the simulations took 4.22 hours using 1024 cores. Table 6 shows the main results. Moltres predicted a  $K_{eff}$  larger than the reference result. The reactivity difference is of 99 pcm. Moltres yields a smaller control rod worth. The difference is of 312 pcm. The axial offset for the Moltres simulation is a 4% higher than the reference result. We attribute the discrepancies to the use of the reflective boundary conditions instead of

the periodic boundary conditions. Once again, section 3.1 discuss further on the use of periodic and reflective boundary conditions.

Figure 20 shows the radially averaged axial power distribution. Moltres results look close in shape and magnitude to the reference results. Figure 21 shows the axially averaged radial power distribution. Moltres results are close to the reference results. Moltres power distribution in the inner ring is larger. The differences are within 0.25 W/cm<sup>3</sup>.

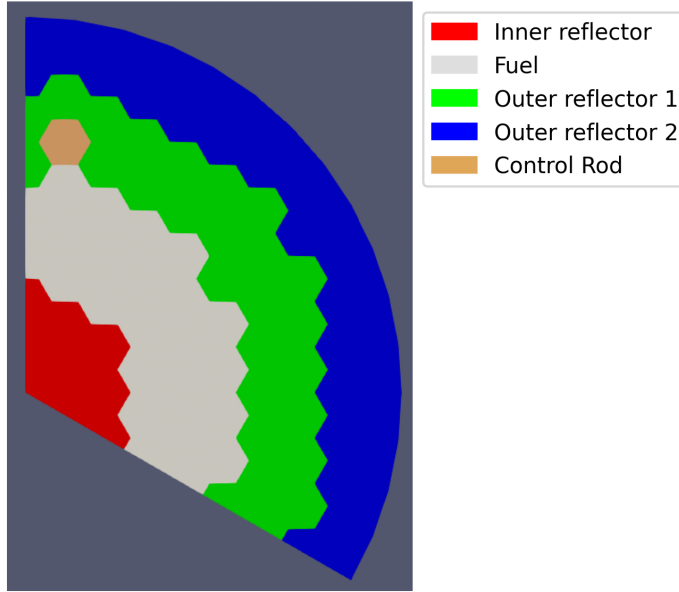


Figure 19: 1/3<sup>rd</sup> of the MHTGR-350 geometry.

Table 6: Global parameters.

Parameter	Benchmark	Moltres
$K_{eff}$	1.06691	1.06804
$\Delta\rho_{CR}$ [pcm]	822.1	509.8
AO	0.168	0.1753

### 3.1 Periodic vs Neumann BCs

In the last section, we observed deviations in Moltres results. In this section, we analyzed the discrepancies that the reflective boundary condition approximation may introduce. As the last section mentioned, the memory requirements of the simulation limit the use of the periodic boundary conditions. To reduce the memory requirements, we collapsed the group constants to a smaller number of energy groups. We simulated two cases: one that uses a 3-group structure and one that uses a 6-group structure. The simulations required two meshes each.

The 3-group simulation had 62118 DoFs/energy-group (total of 186354 DoFs) and 61596 DoFs/energy-group (total of 184788 DoFs) for the control rod out and control rod in cases, respectively. The 6-group simulation had 16898 DoFs/energy-group (total of 101388 DoFs) and 19116 DoFs/energy-group (total of 114696 DoFs) for the control rod out and control rod in cases, respectively. We highlight that the 6-group simulation had to use a coarser mesh, otherwise it would not run. This confirms the suspicion that the simulation's memory requirements prevents it from running.

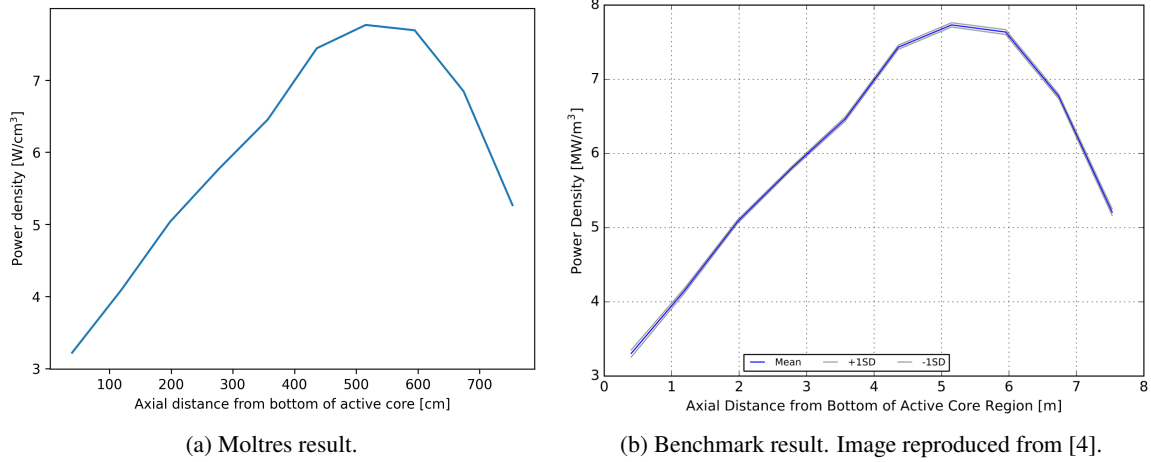


Figure 20: Radially averaged axial power distribution.

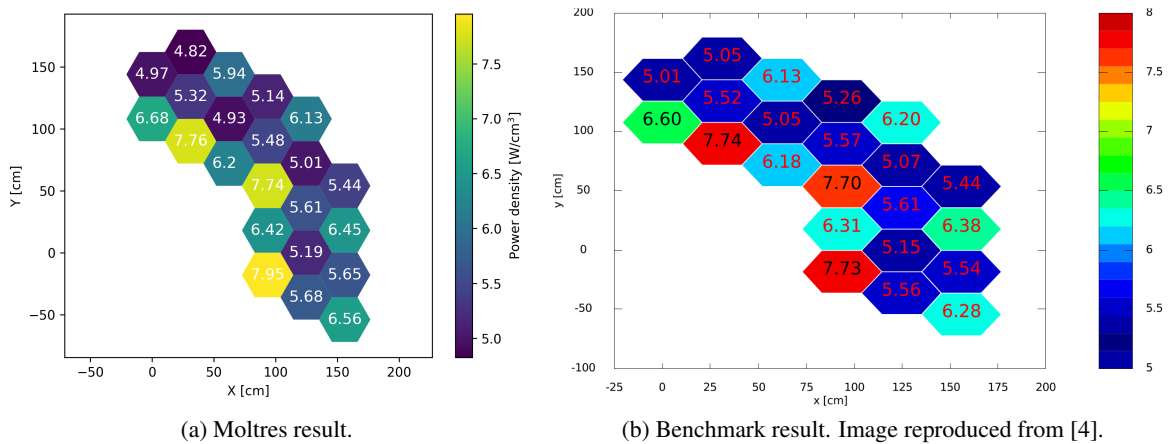


Figure 21: Axially averaged radial power distribution.

For both cases, we ran simulations with periodic and neumann boundary conditions and we compared their results. Table 7 presents the results. The neumann boundary condition increases the  $K_{eff}$ . For the control rod out case, the increase is small. However, for the control rod in case, the increase is considerable. The combined effect of both increases leads to a decrease in the control rod worth. The axial offset results almost unaffected by the boundary condition approximation.

Table 7: Global parameters comparison for different types of BCs.

Energy groups	Type of BCs	$K_{eff,out}$	$K_{eff,in}$	$\Delta\rho_{CR}$ [pcm]	AO
3	Periodic	1.07571	1.06776	692.6	0.237
	Neumann	1.07586	1.07021	490.5	0.237
6	Periodic	1.07182	1.06356	724.3	0.185
	Neumann	1.07197	1.06610	513.3	0.186

## 4 Conclusions

The preliminary studies focused on several aspects of the simulations. The first aspect was the effect of distributing homogeneously the fuel compact isotopes in the Serpent model. The heterogeneous calculation took 28% more time. The results showed that the multiplication factor decreases considerably. Additionally, the homogenization of the fuel compact appears not to have a strong impact over the group constants. However, the considerable difference in the multiplication factor suggests that the combined effect of small variations in the group constants is significant. Although the particles' explicit modeling is time-consuming, it results necessary.

Focusing on a fuel column of the MHTGR-350, we investigated the effects of the energy group structure on the diffusion calculations. We considered four different operational cases: a fuel column without LBPs and a fuel column with LBPs, both cases at 600K and 1200K. Serpent obtained the homogenized group constants of the fuel column. Moltres took such constants as input with a Gmsh mesh. The first study compared the Moltres axial flux to Serpent axial flux. Moltres used a 26 energy group structure to run the simulations. Overall, the axial fluxes were close in shape and magnitude. A different study focused on the effects of the energy group structure on the  $K_{eff}$ . We note that the number of energy groups does not affect the accuracy of the eigenvalue calculations in Moltres. We also compared the  $L_2$ -norm relative error of the axial flux in the active core using different energy group structures. For the four operational cases, the accuracy improves increasing the number of energy groups. Additionally, we presented the simulation computational expense for the different number of energy groups. The simulation time and memory requirement rises increasing the number of energy groups. We notice as well that the computational time increases for the fuel column with LBPs. Finally, we analyzed the impact of using different 15-group structures on the  $L_2$ -norm relative error of the axial flux. We chose the 15d structure as the best performing.

Based on the results from the fuel column analysis, we compared Moltres full-core results to Serpent reference results. We considered two operational cases: 600K and 1200K. Serpent obtained the homogenized group constants of the different regions of the reactor. Moltres took such constants as input with a Gmsh mesh. The first analysis compared the Serpent and Moltres eigenvalues. Moltres results were bigger. The overall difference was less than 300 pcm. The second analysis compared the radial power distributions from both codes. These results showcase the symmetry of the problem. To reduce the computational expense other simulations could reduce the problem size by a half. Overall, Moltres radial power distribution shows close proximity to the Serpent's result. We also compared the flux shape and magnitude. The axial fluxes show small discrepancies, mostly in their magnitude. The radial fluxes are close in shape and magnitude. However, the radial flux in the diffusion calculation fails to capture the steep flux close to the LBPs. Overall, the fluxes are similar.

The simulation capabilities for HTGRs has not reached the state of the art of LWRs. This delay in the

development of such capabilities has motivated OECD/NEA to define a benchmark to carry out code-to-code comparisons. The benchmark uses the MHTGR-350 as the reference design. We conducted Phase I Exercise 1 with Moltres. The benchmark defines the group constants for the exercise. The group constants have a 26-energy group structure. The benchmark exercise sets periodic boundary conditions on the the sides of the geometry. Such implementation in Moltres has been challenged by the simulation high memory requirements. To go around such barrier, we approximated the periodic boundary condition with a reflective boundary condition. Two out of three global parameters exhibit good agreement with the reference results. However, the control rod worth presents a large discrepancy. Such a discrepancy rises from the approximation in the boundary conditions. The use of a reflective boundary condition for the control rod out case does not have a strong impact over the  $K_{eff}$ . On the other hand, the choice of boundary condition for the control rod in case has a substantial effect. The combined effect of the approximation leads to large error in the control rod worth. The approximation has a small influence on the axial offset.

## References

- [1] Christophe Geuzaine and Jean-François Remacle. Gmsh: a three-dimensional finite element mesh generator with built-in pre- and post-processing facilities., June 2020.
- [2] Alexander Lindsay, Gavin Ridley, Andrei Rykhlevskii, and Kathryn Huff. Introduction to Moltres: An application for simulation of Molten Salt Reactors. *Annals of Nuclear Energy*, 114:530–540, April 2018.
- [3] G Marleau, A Hebert, and R Roy. A USER GUIDE FOR DRAGON VERSION4. page 318, 2016.
- [4] OECD NEA. Coupled Neutronic/Thermal- Fluid Benchmark of the MHTGR-350 MW Core Design: Results for Phase I Exercise 1, February 2020.
- [5] Mateusz Pater. Multiphysics simulations of Molten Salt Reactors using the Moltres code. Master’s thesis, Universite Paris-Saclay, Copenhagen, Denmark, September 2019.